Thermofluidic Characteristics of a Porous Ventilated Brake Disk

Article *in* Journal of Heat Transfer · February 2015

DOI: 10.1115/1.4028864

7 authors, including:

Hongbin Yan
Northwestern Polytechnical University
10 PUBLICATIONS **31** CITATIONS
SEE PROFILE

Kiju Kang
Chonnam National University
122 PUBLICATIONS **1,204** CITATIONS
SEE PROFILE

Tian Jian Lu
Xi'an Jiaotong University
551 PUBLICATIONS **8,635** CITATIONS
SEE PROFILE

Frank Kienhofer
University of the Witwatersrand
15 PUBLICATIONS **25** CITATIONS
SEE PROFILE

H. B. Yan
School of Energy and Power Engineering,
Xi'an Jiaotong University,
Xi'an 710049, China
e-mail: hongbinyanhb@163.com

T. Mew
School of Mechanical Engineering,
University of the Witwatersrand,
Johannesburg 2050, South Africa
e-mail: timdmew@gmail.com

M.-G. Lee
Department of Mechanical Systems Engineering,
Chonnam National University,
Gwangju 500-757, South Korea
e-mail: kkameoe@naver.com

K.-J. Kang
Department of Mechanical Systems Engineering,
Chonnam National University,
Gwangju 500-757, South Korea
e-mail: kjkang@chonnam.ac.kr

T. J. Lu
State Key Laboratory
for Mechanical Structure Strength and Vibration,
School of Aerospace,
Xi'an Jiaotong University,
Xi'an 710049, China
e-mail: tjlu@mail.xjtu.edu.cn

F. W. Kienhöfer
School of Mechanical Engineering,
University of the Witwatersrand,
Johannesburg 2050, South Africa
e-mail: frank.kienhofer@wits.ac.za

T. Kim[1]
School of Mechanical Engineering,
University of the Witwatersrand,
Johannesburg 2050, South Africa
e-mail: tong.kim@wits.ac.za

Thermofluidic Characteristics of a Porous Ventilated Brake Disk

We introduce a new class of ventilated brake disk which incorporates an open cellular core: wire-woven bulk diamond (WBD). Transient and steady-state thermofluidic characteristics are presented. As reference, a commercially available pin-finned brake disk is also considered. At a braking power of 1.9 kW, representative of a medium sized truck descending a 2% gradient at a vehicle speed of 40 km/h (i.e., 200 rpm), the WBD cored brake disk reduces the overall brake disk temperature by up to 24% compared to the pin-finned brake disk. Results also reveal that in typical operating ranges (up to 1000 rpm), the WBD core provides up to 36% higher steady-state overall cooling capacity over that obtainable by the pin-finned core. In addition, the three-dimensional morphology of the WBD core gives rise to a tangentially and radially more uniform temperature distribution. Although the WBD core causes a higher pressure drop, this is balanced by the benefit of a stronger suction of cooling flow. Flow mixing in an enlarged heat transfer area by the WBD core is responsible for the substantial heat transfer enhancement. The WBD core is mechanically strong yet light while providing a substantial reduction in a brake's operating temperature. [DOI: 10.1115/1.4028864]

Keywords: fluid flow, heat transfer, ventilated brake disk, pin fins, WBD

1 Introduction

Vehicle braking systems transform large amounts of kinetic energy into heat using sliding friction between brake disks and pads (Fig. 1(*a*)). During high-load braking, such as repeated high-speed braking or extended downhill braking, the temperature at the friction interface can be high [1]. Previous studies have shown that such high operating temperature can cause brake fade [2,3] and increased wear of the rubbing surfaces [4]. It has also been reported that if the operating temperature is too high (above 600 °C) [5], the brake fluid may boil in the calliper cylinder, leading to "fluid fade" [6]. Furthermore, brake disk temperature distributions are nonuniform and the consequent nonuniform thermal deformation of the brake disk causes disk cracking [7] and thermal judder [8], which is aggravated by high temperatures. Therefore, sufficient and uniform cooling of the brake disk is desirable to improve braking performance and safety.

Brake disks are, therefore, often designed with two rubbing disks sandwiching various heat dissipation elements. These "vented or ventilated brake disks" draw cooling flow into the ventilated channel when the brake disk rotates [9]. Thus, substantially lower brake disk temperatures can be achieved using forced convection in the ventilated channel. Several different types of heat dissipation elements including purely radial vanes, curved vanes and pin fins have been proposed and employed in commercially available ventilated brake disks as illustrated in Fig. 1(*b*).

Johnson et al. [9] measured the velocity field around a ventilated brake disk equipped with purely radial vanes in its ventilated channel. They found that the cooling flow swirls in the counter-rotating direction with respect to the brake disk axis before entering the ventilated channel. Due to the Coriolis effect, the incident flow angle to the vane passage becomes high, causing flow separation from the leading edge of the vanes. Consequently, a large flow recirculation region forms on the suction side of each vane, which reduces the amount of cooling flow in the ventilated channel [10–13].

To increase the mass flow rate of cooling flow in the ventilated channel, some improved vane designs have been devised such as

[1]Corresponding author.
Contributed by the Heat Transfer Division of ASME for publication in the JOURNAL OF HEAT TRANSFER. Manuscript received October 1, 2013; final manuscript received October 15, 2014; published online November 18, 2014. Assoc. Editor: Wei Tong.

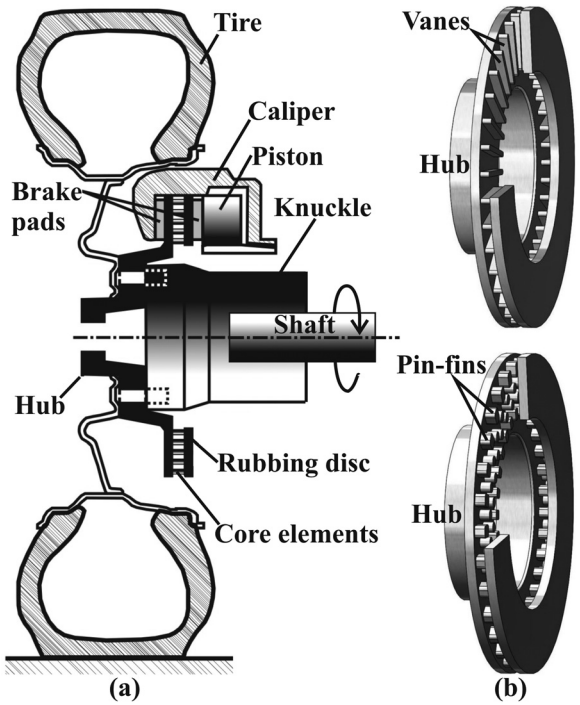

Fig. 1 Schematics of a disk brake system: (*a*) components and (*b*) current ventilated brake disks with vanes and pin fins

curved vanes which suppress flow separation. As a result, the mass flow rate and the corresponding cooling performance are reported to be further improved [14,15]. However, the highly nonuniform heat transfer caused by the circumferentially distributed vanes leads to a large temperature gradient in the disks near the vanes [12,16,17]. Corresponding thermal stresses make such brake disks prone to thermal fatigue cracking along the vanes [17], which has restricted their application.

Subsequently, brake disks with pin fins that are both "radially" and "circumferentially" distributed in the ventilated channel were developed to reduce large temperature gradients within the disks. Wallis et al. [16], Wallis [17] numerically investigated brake disks with diamond and teardrop cross-sectioned pin fins and obtained a more uniform temperature distribution. Parametric studies were conducted by Palmer et al. [18,19] to further improve the heat transfer performance of such brake disks.

Although vanes and pin fins have, to an extent, been shown to improve the heat transfer performance of the brake disks, constraints by the casting method make it difficult to optimize every aspect of the design. To eliminate casting defects, vanes and pin–fins in current ventilated brake disks are prismatic and thick, configured two-dimensionally normal to the rubbing disks. This configuration may not be favorable for forced convective heat transfer due to limited flow mixing and heat transfer area. Such a situation motivates the authors to introduce recently developed novel heat dissipation elements into a ventilated brake disk to further improve its cooling performance.

In this study, we introduce a new heat dissipation medium as the core of a ventilated brake disk. This WBD material is lightweight and highly porous but mechanically strong. Thermofluidic characteristics of this new porous ventilated brake disk are presented with a direct comparison to a commercially available pin-finned brake disk, laying the foundation for an improved WBD brake disk to be presented as future work. To this end, a series of experiments in stationary and rotating conditions were conducted.

2 WBD Cored Ventilated Brake Disk

Various periodic cellular materials with tetrahedral, pyramidal, and Kagome unit cells have been recently developed [20–22]. A multitude of studies have shown that such materials have excellent specific strength/stiffness [20] as well as heat dissipation capability [23–25], making them a good candidate material for lightweight ventilated brake disks where simultaneous thermal and mechanical load bearing capabilities are required. In this study, a ventilated brake disk with a WBD core is investigated.

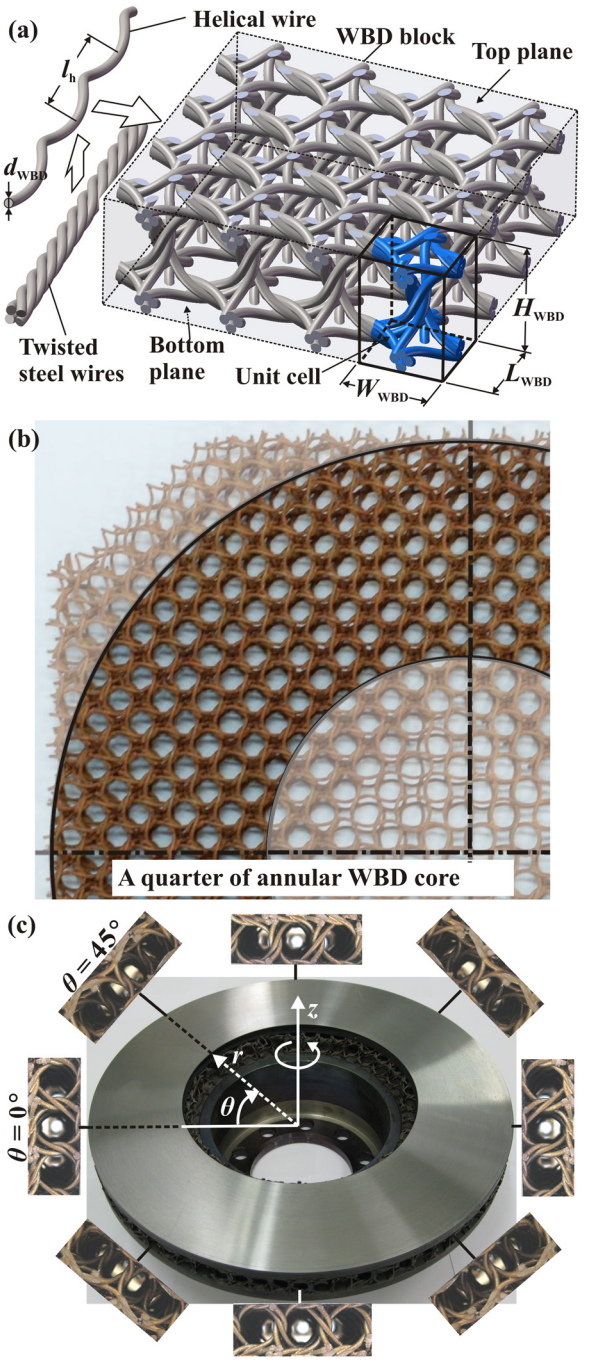

Fig. 2 WBD and its integration into a ventilated brake disk: (*a*) fabrication of WBD and its morphology; (*b*) a quarter of an annular WBD core; (*c*) a WBD brake disk showing aerodynamic anisotropy

A single layered metallic WBD block and its fabrication procedures are schematically illustrated in Fig. 2(*a*). First, four straight steel wires with an identical diameter (d_{WBD}) are twisted together until plastic deformation occurs and then untied from one another to form identical helical wires with a helical pitch, l_h. Next, the helical wires are weaved in two mutually perpendicular in-plane directions to form two-dimensional square meshes with an edge

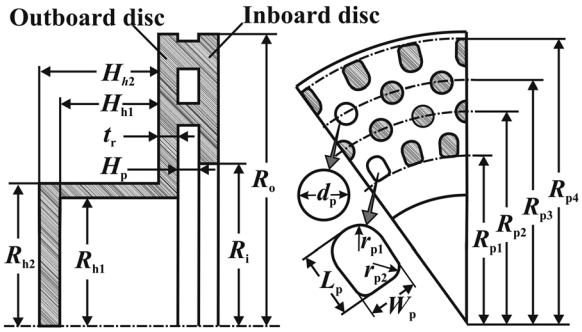

Fig. 3 Geometric details of the pin-finned brake disk showing three periods of the core topology

length of the square hole set to $0.5l_h$. Afterward, two square meshes are parallel fixed in the bottom and top planes indicated in Fig. 2(*a*) at a constant interval of $l_h/(2)^{1/2}$ with the aid of a fixing frame. Additional helical wires are then screwed into the square meshes in four different out-of-plane directions (with an included angle of 45 deg to one another) at an angle of 45 deg relative to the bottom and top planes to form a specific topology. Finally, the intersecting points of the helical wires are sprayed with copper paste (Cubond^{TM} grade 17LR, from SCM Metal Products, Inc.) and brazed at 1120 °C in a de-oxidation atmosphere of H_2–N_2 mixture. The bonding significantly improves the thermomechanical performance of the WBD compared with unbrazed WBD cores [25]. Further details of the fabrication procedure can be found in Refs. [21,22]. The single-layered WBD block is subsequently cut into an annular shape (Fig. 2(*b*)). After which, the WBD core is sandwiched by and brazed on to two mild steel rubbing disks (Fig. 2(*c*)).

3 Experimental Details

3.1 Brake Disk Samples. A commercially available pin-finned brake disk made of cast iron (manufactured by Alfa International (Pty) Ltd) was tested as reference. The brake disk contains four rows of pin fin elements sandwiched between two rubbing disks. The two central rows of the pin fins have a circular cross section, while the innermost and outermost rows of pin fins have a blunt end as shown in Fig. 3. In total, 120 pin fins are arranged with 30 pin fins in each row. The pin fins occupy approximately 30% of the total volume of the ventilated channel, resulting in a porosity of ~0.7 and a surface area density of ~81 m^2/m^3. Detailed dimensions of the samples are summarized in Table 1.

Two separate WBD brake disks were fabricated. Two annular WBD cores (Fig. 2(*b*)) were first fabricated using cold-rolled mild steel helical wires (SAE1006B) with the diameter of $d_{WBD} = 1.5$ mm and the helical pitch of $l_h = 19.0$ mm. One WBD core was then brazed on to two mild steel (SAE1006) rubbing disks (for testing on a rotating rig), while the second core was brazed onto a single mild steel rubbing disk (for stationary testing).

Table 1 Detailed dimensions of the pin-finned brake disk

Parameter	Value	Parameter	Value
d_p	12.5 mm	R_i	93.0 mm
H_{h1}	56.5 mm	R_o	168.0 mm
H_{h2}	68.5 mm	R_{p1}	96.0 mm
H_p	12.0 mm	R_{p2}	121.5 mm
L_p	13.5/16.0 mm	R_{p3}	139.0 mm
r_{p1}	5.0/6.0 mm	R_{p4}	163.5 mm
r_{p2}	3.0/3.0 mm	t_r	11.0 mm
R_{h1}	73.0 mm	W_p	10.0/12.0 mm
R_{h2}	82.0 mm		

The unit cell of the WBD core is highlighted in Fig. 2(*a*). The overall dimensions of the unit cell are: $L_{WBD} = 13.4$ mm, $W_{WBD} = 13.4$ mm, and $H_{WBD} = 14.0$ mm. The porosity and surface area density of the WBD core were respectively estimated to be ~0.9 and ~255 m^2/m^3 using the following formulae for the idealized diamond unit cell [22]:

$$\varepsilon = 1 - 3\sqrt{2}\pi\left(\frac{d_{WBD}}{l_h}\right)^2 \quad (1)$$

$$\rho_{SA} = 12\sqrt{2}\pi\frac{d_{WBD}}{l_h^2} \quad (2)$$

where ε and ρ_{SA} are the porosity and the surface area density of the WBD core, respectively. The helical (instead of the idealized straight) ligaments increase the relative density $(1 - \varepsilon)$ and surface area density by ~15%, which needs to be accounted for. The equivalent yield strength, maximum strength, and Young's modulus of the core were measured to be 3.2 MPa, 4.8 MPa, and 1.08 GPa, respectively. Other dimensions of the WBD brake disks are identical to those of the pin-finned brake disks.

3.2 Test Facilities. Three separate test rigs were constructed; each serves different purposes. A stationary test rig (Fig. 4) was used to characterize pressure drop and local endwall heat transfer distribution. Two rotating test rigs were used to investigate transient and steady-state overall cooling performance (Fig. 5(*a*)) and steady-state thermofluidic characteristics and cooling flow rate (Figs. 5(*b*) and 5(*c*)).

3.2.1 Stationary Test Rig. Figure 4 schematically illustrates the stationary test rig consisting of a plenum chamber where air is supplied by a centrifugal blower. After the chamber, flow passes through a circular intake duct ($D_{duct} = 60$ mm), in which wire screens and honeycombs were installed. Flow then enters another smaller plenum chamber to minimize flow separation at the inlet of the ventilated channel caused by an abrupt turning from axial to radial directions and diverges through an annular flow channel

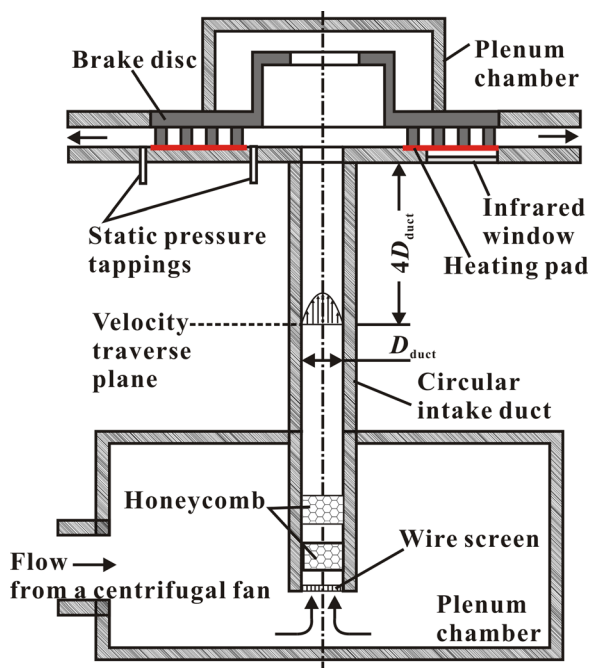

Fig. 4 Stationary test setup for pressure drop and heat transfer measurements

(outer diameter 500 mm). To eliminate flow leakage, the smaller plenum chamber and annular top endwall were attached to the brake disk. Mass flow rate was controlled by an inverter connected to the centrifugal blower.

3.2.2 Rotating Test Rigs. The rotating test rig shown in Fig. 5(*a*) consists of an ac motor mounted on a base frame, which is connected to a shaft through a gearbox and a flexible coupling. The shaft rotates on bearings, and is flanged at the opposite end to allow brake disks to be directly attached. A pneumatic brake caliper applies a braking torque to the disk. The braking pressure and motor speed can, respectively, be controlled using an electronically controlled Festo pressure regulator and SEW-Eurodrive frequency inverter.

Another rotating test rig shown in Fig. 5(*b*) was constructed to characterize steady-state thermal behavior of the pin-finned and WBD brake disks. It has a similar arrangement with the braking test rig with an ac motor, a flexible coupling, bearings, shaft, and flange. A knuckle (outer diameter 127 mm) was bolted onto the flange together with the brake disk. Another shaft supported by two bearings and the knuckle is used to allow a slip ring to be mounted. The slip ring has four channels and connects the heating elements attached to the brake disk surfaces with the DC power supply. The heating elements are used to simulate the frictional heating by the brake pads. The rotational speed of the brake disk was controlled by an inverter connected to the ac motor and measured by a tachometer.

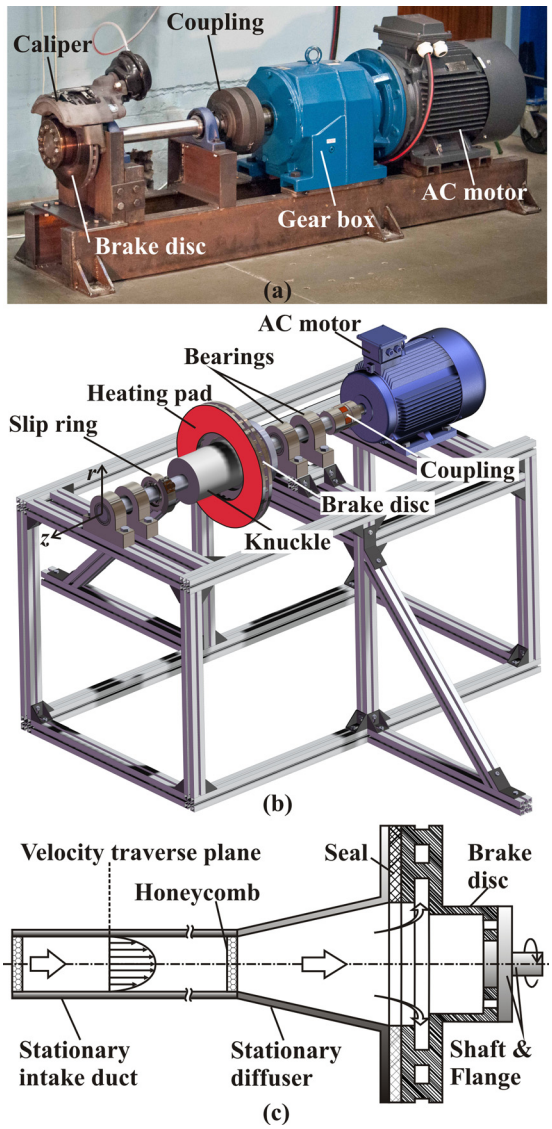

Fig. 5 Rotating test setup: (*a*) for transient heat transfer measurement and braking test; (*b*) for steady-state heat transfer measurement; and (*c*) test section for cooling flow rate measurement

3.3 Stationary Test Details

3.3.1 Velocity and Pressure Drop Measurements. To measure the mass flow rate of the cooling flow entering the stationary ventilated channel, the profile of axial velocity component at $4.0D_{duct}$ upstream the brake disk was radially traversed using a stagnation probe (having the outer diameter of 0.4 mm) with a static pressure tapping flush mounted on the flow tube (having the inner diameter of 60 mm). Then, the velocity profile was integrated to calculate mass flow rate. The nearest measurement point was located at 0.2 mm away from the inner surface of the flow tube (i.e., 0.33% of the flow tube diameter). Based on the measured velocity profile, the mean velocity (U_m) in the intake duct was calculated and correlated as a function of the duct centerline velocity (U_c) as

$$U_m = 0.8881U_c - 0.2086 \tag{3}$$

The mean velocity U_{in} at the inlet of the ventilated channel was then calculated as

$$U_{in} = U_m \frac{\pi R_{duct}^2}{A_{in}} \tag{4}$$

where $A_{in} = 2\pi R_i H_p$ for the pin-finned brake disk and $A_{in} = 2\pi R_i H_{WBD}$ for the WBD brake disk; R_{duct} is the inner radius of the circular intake duct. The inlet velocity (U_{in}) was set to vary from 2.1 m/s to 11.4 m/s to cover the typical flow ranges in the ventilated brake disk during actual braking [16,26,27].

To characterize the aerodynamic anisotropy of the pin fin and WBD cores, the mid-height radial velocity (U_o) at the outlet of the ventilated channel was azimuthally traversed using a Pitot probe.

Static pressure tappings were used to measure the pressure drop. One pressure tapping was placed 10.0 mm upstream and the other 10.0 mm downstream the ventilated channel (Fig. 4). The cores of both the brake disks have periodic topologies: 90 deg for the WBD (see Fig. 2(*c*)) and 12 deg for the pin fins (see Fig. 3). For each sample, the assembly composed of the brake disk, top endwall, and plenum chamber was rotated in 1 deg increment within these periods to allow azimuthal pressure profiles to be measured. The static pressures at the inlet and outlet of the ventilated channel were averaged to calculate the overall pressure drop across each core.

3.3.2 Heat Transfer Measurement. To examine thermal uniformity on an inner endwall of the ventilated channel cored by the WBD and the pin fins, the endwall temperature distribution at the inboard side was mapped by a precalibrated infrared (IR) camera. To this end, annular film heating elements were first attached to the pin-finned and WBD cores using a 0.1 mm thick thermally conductive tape with a thermal conductivity of 1.5 W/(mK) (see Fig. 4). The heating elements are composed of etched Inconel heating wires (thickness 0.0476 mm, thermal conductivity 11.0 W/(mK) [28]) sandwiched between two layers of Kapton films (thickness 0.0762 mm, thermal conductivity 0.12 W/(mK) [29]). A 10 mm thick Perspex disk was attached to the outer surface of the heating elements to support the sample. The endwalls were covered by a thick thermal insulation material to minimize heat loss.

An IR camera (FLIR^{TM} T640) was then used to monitor the outer surface temperature of the heating elements which were painted black to reduce reflectivity. A heating section of the bottom acrylic endwall was removed to allow an IR window (Edmund Optics Inc.) to be installed. Thus, a 10 mm thick air gap

was formed between the heating elements and the IR window to minimize heat loss. Detailed operating conditions are listed in Table 2.

3.4 Rotating Test Details

3.4.1 Transient Braking Test. The braking test simulated a representative medium sized truck (total mass 3600 kg with all four wheels braking in equal proportion) descending a 2% gradient at a speed of 40 km/h (i.e., 200 rpm). The braking pressure was adjusted throughout the tests to ensure that the output power of the ac motor was kept steady at 1.9 kW for both the brake disks. Detailed operating conditions are listed in Table 2.

The transient behavior of the outer surface temperature of the outboard rubbing disk was recorded using the IR camera during braking. Before the test, the IR camera was calibrated for the ductile cast iron and mild steel surfaces. For calibration, three film T-type thermocouples were mounted flush on each disk surface. Each disk was then heated up to 200 °C. The emissivity in the IR camera was then adjusted until the temperature readings matched those from the thermocouples.

3.4.2 Steady-State Heat Transfer Measurement. During braking, heat generated by frictional heating is transferred into the brake disk through the rubbing disks, and is simultaneously removed by the surrounding fluid flow. The actual heat (flux) distribution on the rubbing disks is unknown but depends on the contact conditions between the rubbing disks and brake pads and wear conditions. Since comparative overall cooling performance of the two brake disk cores is of concern under identical contact conditions, constant and identical levels of heat flux were imposed by the annular film heating elements attached to the outer surfaces of both rubbing disks. Aluminum (Al) foils (thickness 0.06 mm) were also attached to the outer surfaces of the heating elements to remedy the nonuniformity of the heat flux that may be caused by gaps between etched heating wires within the heating elements. The temperature of the inboard Al foil was recorded by the IR camera which was calibrated in situ using a foil type thermocouple (Omega^{TM}). The Al foil was painted black to reduce reflectivity. In addition, a bead type thermocouple (Omega) was used to measure the ambient air temperature. Detailed operating conditions are listed in Table 2.

3.4.3 Flow and Pressure Measurements. Cooling flow entering the rotating ventilated brake disk was visualized using illuminated neutrally buoyant helium bubbles. The bubbles were produced by mixing a film producing soap solution with helium in a mixing nozzle. Clean air was used as a carrier fluid and was mixed with the bubbles in a cylindrical vortex chamber. The bubbles, measured between 1 mm and 3 mm, demonstrated resilience against impact at stagnation points on the brake disk in the flow, with very few bubbles bursting. A modulated arc lamp was used to illuminate the bubbles while photographing.

The mass flow rate of cooling flow drawn into the ventilated channel was measured to characterize the pumping capacity of each brake disk. To facilitate its measurement, a small angle diffuser was connected to the inlet of the ventilated brake disk and preceded by a circular intake duct ($D_{duct} = 100$ mm) as shown in Fig. 5(*c*). A closed-cell foam type layer was tightly sandwiched between the rotating brake disk and the stationary diffuser to minimize possible flow leakage. The axial velocity component was radially traversed by a Pitot tube with the outer diameter of 3.0 mm in the flow tube having the inner diameter of 100 mm, which was then integrated to calculate mass flow rate. The nearest measurement point was located at 5.0 mm away from the inner surface of the flow tube (i.e., 5.0% of the flow tube diameter). Figure 6 shows measured velocity profiles at various disk rotational speeds. The results indicate that the developing flow patterns in the circular duct are symmetric with respect to the duct axis. Similar profiles were obtained for both the brake disks. Mass flow rate of the cooling flow was then calculated by integrating each velocity profile and correlated for both the brake disks as

$$\dot{m} = 2.6 \times 10^{-5} N (N \leq 1000\,\text{rpm}) \tag{5}$$

where $\dot{m}$ is the mass flow rate of cooling flow for both brake disks, and N refers to the rotational speed of the brake disk in rpm. Equation (5) indicates a linear increase of the mass flow rate with the rotational speed, which is consistent with previous experimental and numerical studies [9,16,26,27,30].

3.5 Data Reduction Parameters. The Reynolds number is defined as a function of the hydraulic diameter (D_h) and mean velocity (U_{in}) at the ventilated channel inlet as

$$\text{Re}_{Dh} = \frac{\rho U_{in} D_h}{\mu} \tag{6}$$

where ρ and μ are the density and dynamic viscosity of cooling fluid (air), respectively. The hydraulic diameter D_h was calculated to be $2H_p$ and $2H_{WBD}$ for the pin-finned and WBD brake disks, respectively. For rotating experiments, the rotational Reynolds number [9] is used and defined as

$$\text{Re}_{Ro} = \frac{\rho \omega R_o^2}{\mu} \tag{7}$$

where ω is the angular velocity of the brake disk. Equation (5) indicates that the two brake disks have the same pumping capacity, drawing the same amount of cooling flow rate into the ventilated channel for a given rotational speed. Hence, the Reynolds number (Re_{Dh}) has the same value for both brake disks for a given rotational Reynolds number (Re_{Ro}).

The overall pressure drop across the pin-finned and WBD cores is characterized by a nondimensional pressure coefficient, the friction factor (f_{Dh}) defined as

Table 2 Operating conditions of heat transfer measurements

Test configuration	Parameter	Value
Stationary heat transfer measurement	Mass flow rate of air	0.0789 kg/s
	Inlet air temperature	23.5 °C
	Heat flux	5787 W/m^2
Transient braking test	Rotational speed	200 rpm
	Ambient air temperature	13.0 °C
	Braking power	1.9 kW
Rotating steady-state heat transfer measurement	Rotational speed	100 rpm–1000 rpm
	Ambient air temperature	16 °C–20 °C
	Heat flux	3034 W/m^2

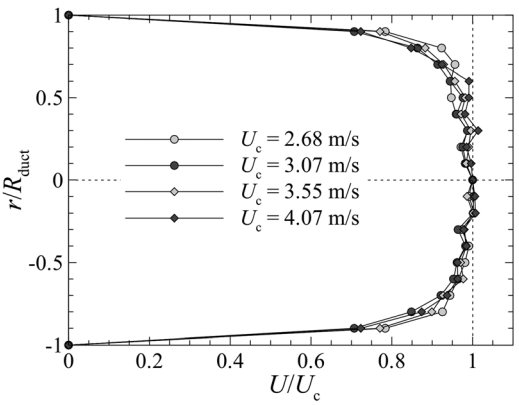

Fig. 6 Measured axial velocity profiles in the circular intake duct normalized by the centerline velocity (U_c)

$$f_{Dh} = \frac{\Delta p}{L}\frac{D_h}{\rho U_{in}^2/2} \tag{8}$$

where Δp is the mean static pressure drop through the cores, L is the radial distance between the two static pressure tappings.

The steady-state overall heat transfer is evaluated by Nusselt number (Nu_{Ro}), defined as

$$Nu_{Ro} = \frac{hR_o}{k} \tag{9}$$

where k is the thermal conductivity of cooling fluid (air) and h is the overall convective heat transfer coefficient defined as

$$h = \frac{q''}{T_{w,m} - T_{amb}} \tag{10}$$

Here, q'' is the heat flux imposed by the heating elements, $T_{w,m}$ is the area-averaged disk surface temperature obtained from the IR images, and T_{amb} is the ambient air temperature.

3.6 Measurement Uncertainties. Pressures were measured by a differential pressure transducer (DSA^{TM}, Scanivalve Inc.) with a resolution of 0.3 Pa. Thus, the measurement uncertainty associated with Reynolds number (Re_{Dh}) and friction factor (f_{Dh}) was estimated using a method reported in Ref. [31] and found to be within 1.4% and 6.7%, respectively. The measured mass flow rate drawn by the ventilated brake disk is relatively low, corresponding to a mean velocity in the circular intake duct varying from 2.35 m/s to 3.40 m/s. Measurement uncertainty of the mass flow rate associated with a typical duct velocity (2.56 m/s) was estimated to be 6.5%. The uncertainty of the disk rotational speed was estimated to be less than 5 rpm, resulting in an uncertainty less than 5% for the rotational Reynolds number (Re_{Ro}).

Ambient air temperature was measured by a T-type thermocouple (Omega) with a resolution of 0.1 °C. During each test, the fluctuation of ambient temperature was measured to be within ±0.4 °C. The temperature measured by the IR camera showed a deviation of ±0.2 °C from that measured by the foil type thermocouple (Omega). Therefore, the uncertainty associated with the mean disk surface temperature was estimated to be within ±0.3 °C. Consequently, the uncertainty for the convective heat transfer coefficient (h) and Nusselt number (Nu_{Ro}) were estimated to be less than 5.2%.

4 Discussion of Results

4.1 Inlet Flow Pattern. As the brake disk rotates, cooling flow is drawn and enters the ventilated channel. Figure 7 shows the flow pattern at the inlet of the brake disk visualized by neutrally buoyant helium bubbles. The helium bubbles were released from a generator placed on the rotation axis upstream the ventilated brake disk. The rotation of the brake disk initiates an outward fluid flow in the ventilated channel. As a result, static pressure at the inlet of the ventilated channel is lowered. Consequently, the suction of ambient air into the channel (as shown by the path lines A and B in Fig. 7) occurs. The apparent centrifugal force continuously drives the air (cooling flow) out of the ventilated channel. In a similar way, ambient air near the outer surface of the rubbing disk is also driven radially outward by the centrifugal force (as indicated by path line C). These flow patterns are consistent with those observed by particle image velocimetry measurement [9]. The flow inside the ventilated channel and over the outer surface of the rubbing disks contribute to the cooling of the brake disk [10].

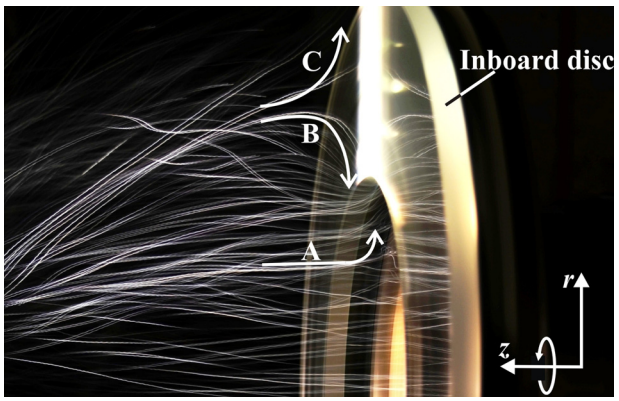

Fig. 7 Inlet flow pattern visualized by helium bubbles

4.2 Transient and Steady-State Cooling Performance. To characterize and compare the cooling performance in a situation as close as possible to representative downhill descending conditions for a medium sized truck, the brake disks were tested at a braking power of 1.9 kW and a rotational speed of 200 rpm as detailed in Sec. 3.4.1.

Figure 8(*a*) compares the surface temperature distribution of the pin-finned and WBD brake disks at selected temporal intervals captured by a precalibrated IR camera. The smooth circumferential distribution of the surface temperature on the rubbing (outboard) disks indicates a good contact between the brake pad and disks. Overall, the surface temperature of the WBD brake disk is lower than that of the pin-finned disk, which clearly demonstrates the efficacy of the WBD core as a new heat dissipation medium incorporated into the ventilated brake disk.

To quantify how the surface temperature of the rubbing disk varies with time, the area-averaged (region (I) indicated in Fig. 8(*a*)) surface temperatures from a series of IR thermal images including those in Fig. 8(*a*) were extracted and plotted in Fig. 8(*b*). After braking is initiated, the surface temperature of both brake disks steeply increases but its rate gradually decreases, finally reaching steady-state values after $t = 4300$ s. In the steady-state regime ($t > 4300$ s) the WBD brake disk exhibits substantially lower surface temperature ($\sim 24.0\%$) than the pin-finned brake disk.

During the initial period ($t < 1000$ s), both brake disks show a similar disk temperature. However, after further braking, the WBD disk provides superior cooling performance and its temperature reduction becomes substantial: 90 °C lower than that of the pin-finned brake disk which operates at 380 °C under the simulated braking conditions.

Figure 8(*c*) presents radial surface temperature profiles extracted from the dashed lines in Fig. 8(*a*) denoted as (II). For both the brake disks, the surface temperature first increases, peaks roughly at $r/R_o = 0.8$ and then decreases with increasing r/R_o. This indicates a better cooling close to the brake hub, which is attributable to the fact that heat generated due to the frictional heating is conducted to the solid hub which acts as an additional extended surface. The slightly decreased surface temperature near the outmost rubbing disk is due to a higher local heat transfer coefficient on the rubbing surface induced by a higher shear stress from the stronger centrifugal force at the larger radius [32]. At $r/R_o > 0.68$, the WBD brake disk has a much lower surface temperature (approximately 100 °C lower at $r/R_o = 0.8$).

4.3 Steady-State Heat Transfer Characteristics. The overall cooling behavior of the commercially available ventilated brake disk having a pin-finned core and the porous WBD brake disk has been compared at 1.9 kW braking power, representative of the field conditions experienced by a medium sized truck descending a 2% gradient at a vehicle speed of 40 km/h (i.e., 200 rpm). However, it is important how such cooling performance is influenced by operating conditions such as vehicle speed (or the

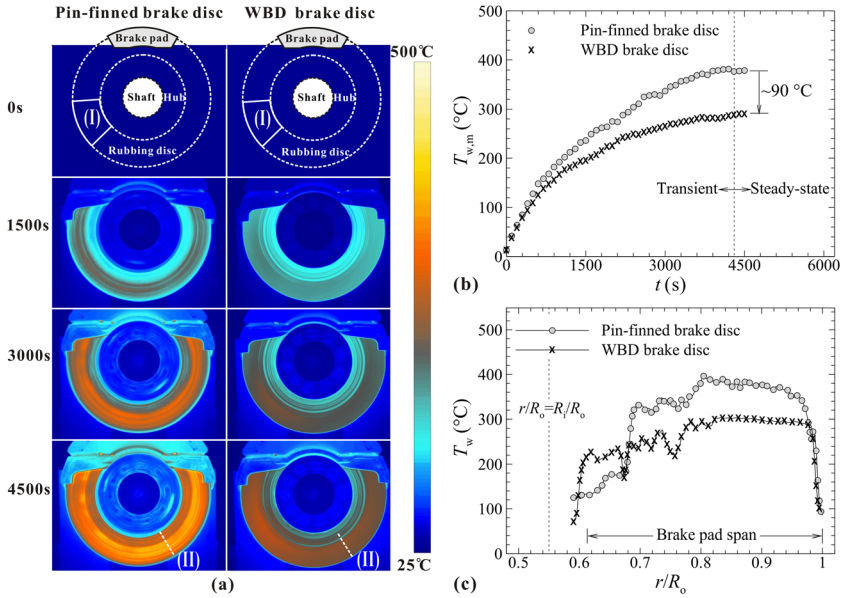

Fig. 8 Comparison of cooling performance of both brake disks, simulating 2% gradient continuous downhill braking at a vehicle speed of 40 km/h (i.e., 200 rpm) and a braking power of 1.9 kW: (*a*) transient local surface temperature; (*b*) transient mean surface temperature; and (*c*) radial temperature profile

rotating speed of the brake disks). To this end, the steady-state overall heat transfer was characterized for a wide range of rotational speeds from 100 rpm to 1000 rpm.

Figure 9(*a*) presents representative disk surface temperature distributions on both brake disks, captured by the IR camera at 1000 rpm. The result demonstrates that the WBD brake disk has a significantly lower surface temperature than the pin-finned brake disk under the steady-state conditions, which is consistent with the braking test results.

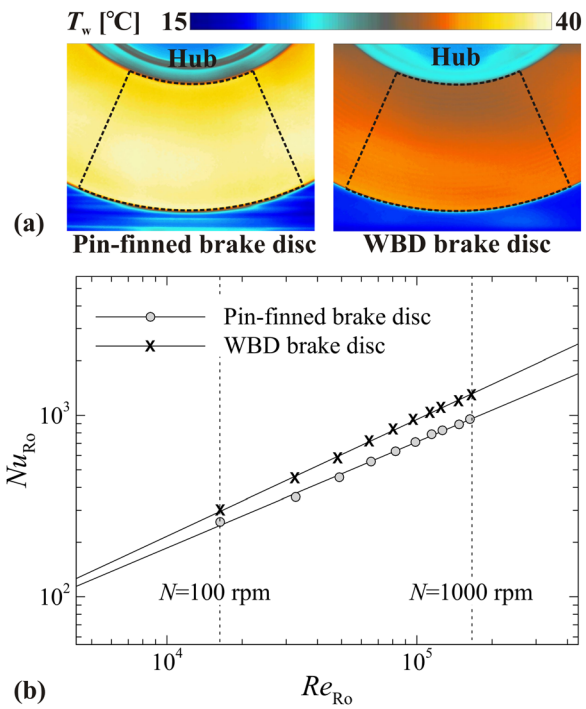

Fig. 9 Measured steady-state heat transfer characteristics: (*a*) surface temperature distribution at 1000 rpm and (*b*) area-averaged Nusselt number with the rotational Reynolds number

The overall convective heat transfer was calculated based on the averaged surface temperature over an area indicated by dashed lines in Fig. 9(*a*). For the rotational speed ranging from 100 rpm to 1000 rpm, the Nusselt number has been correlated as a function of the rotational Reynolds number as

$$\mathrm{Nu}_{\mathrm{Ro}} = C\mathrm{Re}_{\mathrm{Ro}}^{n} \tag{11}$$

where $C = 0.8609$ and $n = 0.5836$ for the pin-finned brake disk; $C = 0.5776$ and $n = 0.6431$ for the WBD brake disk. The Nusselt number for both the brake disks increases monotonically with the rotational Reynolds numbers. The WBD brake disk outperforms the pin-finned brake disk, providing ~16% (at 100 rpm) to ~36% (at 1000 rpm) more heat removal. At 200 rpm, the WBD core is shown to remove 27% more heat than that achievable by the pin–fins, which agrees well with the observed 24% reduction of the rubbing disk temperature in Fig. 8(*b*).

The WBD core has a much larger surface area density (~255 m^2/m^3) than the pin fin arrays (~81 m^2/m^3), which, in part, contributes to the observed substantial enhancement of overall heat transfer.

4.4 Thermal Uniformity. Minimizing the thermal gradients or maximizing the thermal uniformity in the rubbing disks is an important brake design consideration. The detailed local temperature distribution on the inner endwall surface of the ventilated channel (for the stationary test) was mapped using the IR camera. Figure 10(*a*) shows the highly nonuniform temperature distribution. The local endwall temperature on and in the vicinity of each pin fin is lower than other regions due to heat conduction to the pin fins. On the other hand, the vertex of the WBD core is much smaller and is distributed more evenly (Fig. 10(*b*)), providing more uniform thermal distribution in the radial and circumferential directions.

Figure 11 quantitatively shows the local temperature data extracted from Fig. 10 along III(a) for the azimuthal profile and III(b) for the radial profile. Azimuthally (Fig. 11(*a*)), less fluctuation of local endwall temperature in terms of magnitude is presented by the WBD core. It is interesting to notice that the endwall temperature difference between regions where the WBD presents the most open (i.e., $\theta = 0$ deg) and most closed (i.e.,

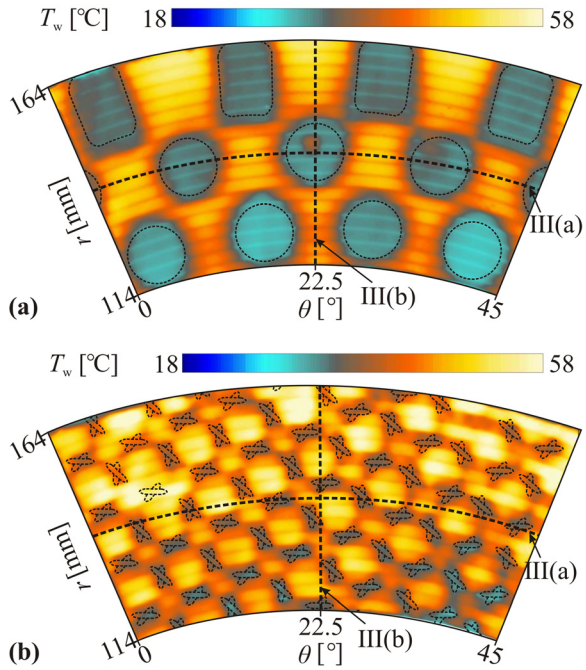

Fig. 10 Measured inner endwall temperature maps by the IR camera for stationary cooling (Re_{Dh} = 14,400): (*a*) the pin-finned disk and (*b*) the WBD disk

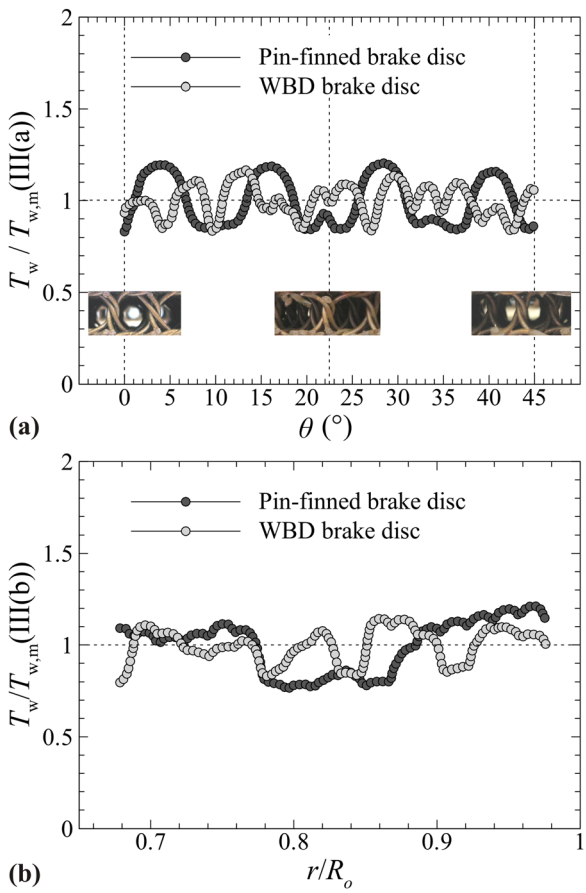

Fig. 11 Measured temperature profiles normalized by mean temperature: (*a*) azimuthal profile (III(*a*)) and (*b*) radial profile at θ = 22.5 deg (III(*b*))

θ = 22.5 deg) flow paths, is insignificant. Radially (Fig. 11(*b*)), there is a slight increase in local temperature toward the outer surface of the pin-finned disk due to the smaller local Reynolds number as the cooling flow is decelerated.

Based on the morphology of the WBD core, highly aerodynamic anisotropy is expected (Fig. 2(*c*)). Figure 12 shows the velocity profile measured at the outlet of the WBD brake disk covering the azimuth angle from θ = 0 deg to 45 deg where the radial velocity (U_o) is normalized by the mean radial velocity ($U_{o,m}$) over the traverse line. The outlet velocity is highly nonuniform, indicating the significant aerodynamic anisotropy. Cooling flow entering the ventilated channel may be uniform but is redistributed according to the flow resistance (or blockage) posed by the morphology of the medium inside the channel [33,34]. With the WBD core, the least flow blockage encountered by the cooling flow is at θ = 0 deg, which provides a preferred flow path whereas the highest blockage exists at θ = 22.5 deg, decreasing cooling flow rate in this flow path. It should be noted that the aerodynamic anisotropy of the pin fins may be negligible compared to the WBD brake disk (Fig. 12).

Although such strong aerodynamic anisotropy exists, the endwall heat transfer distribution on the WBD disk is seen to be highly uniform. It is thought that cooling flow that convects along the more open flow path has higher momentum. This increased local Reynolds number, leads to more heat removal. On the other hand, cooling flow which has the least momentum convecting along the more closed flow path experiences a high level of flow mixing promoted by the WBD ligaments. The combination of these two different mechanisms is believed to provide the observed uniformlike endwall heat transfer (or temperature) distributions. Such thermofluidic characteristics are expected to be applicable under the rotating environment due to the strong dependence of the convective flow and heat transfer on the morphology of the WBD. Furthermore, the endwall thermal distributions in Figs. 10 and 11 also imply that smaller local temperature gradient on the WBD disk surface minimizes thermal stresses within the rubbing disks.

4.5 Heat Transfer Enhancement by the WBD Core

4.5.1 Pressure Drop and Suction Capability. In ventilated brake disks, cooling flow which removes heat from heat dissipation elements in forced convection is drawn by the apparent centrifugal force when the brake disk rotates. To draw more cooling flow into the ventilated channel, a low pressure drop across the core medium is desirable.

Pressure drop across the stationary pin-finned and WBD brake disks has been measured at a wide range of mass flow rates. Figure 13(*a*) shows the pressure drop across each core varying

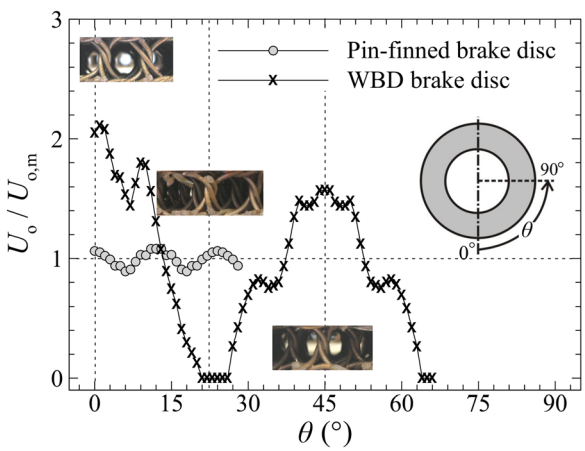

Fig. 12 Measured exit radial velocity profile indicating strong flow anisotropy through the WBD core (Re_{Dh} = 14,400)

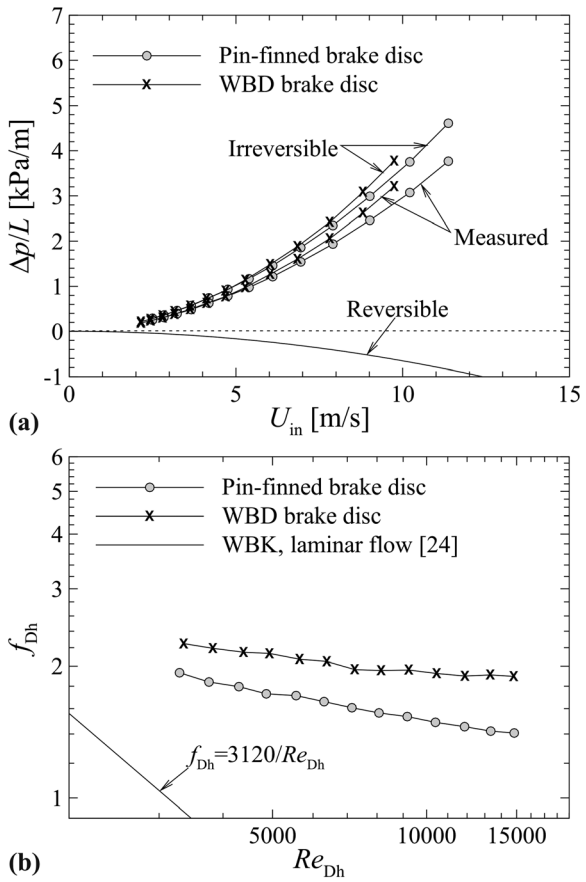

Fig. 13 Pressure drop characteristics for both stationary brake disks: (*a*) pressure drop versus coolant inlet velocity and (*b*) friction factor versus Reynolds number

with the cooling flow velocity at the inlet of the ventilated channel. A monotonic increase in pressure drop with the cooling flow velocity and a higher pressure drop from the WBD compared with the pin fins over the entire velocity range considered are evident. Since the ventilated channel is divergent along the r-axis, there is a pressure recovery opposite to the irreversible pressure loss. Consequently, the measured pressure drop contains both reversible and irreversible pressure components.

To obtain the true pressure loss through the core, the reversible pressure recovery is estimated as

$$\Delta p_r = \frac{\rho U_{in}^2}{2}\left[\left(\frac{R_i}{R_{in}}\right)^2 - \left(\frac{R_i}{R_{out}}\right)^2\right] \tag{12}$$

where R_{in} and R_{out} are the radial locations of two pressure tappings placed at the inlet and outlet of the ventilated channel, respectively. The reversible pressure recovery constitutes about 20% of the measured pressure drop, acting favorably to decrease the pressure loss.

The measured pressure data are replotted in the nondimensional form, the friction factor in Fig. 13(*b*). The friction factor for laminar flow through wire-woven bulk Kagome (WBK) [24] which has a similar topology and porosity is included for comparison. Based on the Reynolds number ranges and the distinguishable slope from the WBK, it may be seen that cooling flow through the WBD and pin-finned brake disks is within the turbulent flow regime. Thus, form drag dominates the pressure loss.

Over the whole range of the Reynolds numbers considered, the pressure drop through the WBD is about 15–30% higher than that through the pin fins. It should be noted that the pin fins occupy

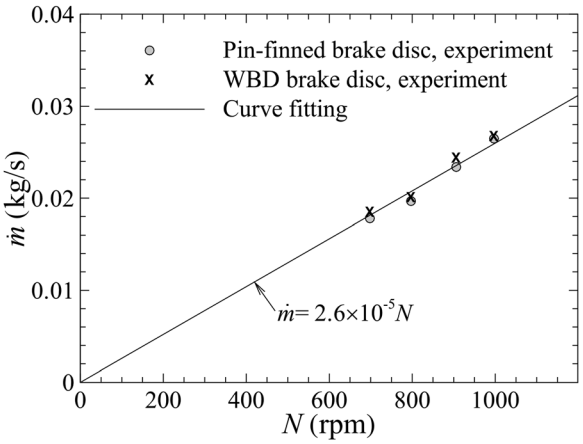

Fig. 14 Pumping capacities of the both brake disks as a function of the brake disk's rotational speed

30% of the total volume of the ventilated channel whereas the WBD takes only about 10% of the total volume. In summary, for a given cooling flow rate, the WBD brake disk causes more pressure drop than the pin-finned brake disk even with approximately 20% less material occupying the flow channel. This high pressure drop results from stronger flow mixing promoted by the highly tortuous flow path presented by the WBD core.

It can be inferred that the higher pressure drop in the WBD core hinders the suction of cooling flow unless the WBD core generates a stronger centrifugal force for a given rotational speed of the brake disk. Figure 14 depicts the cooling flow's mass flow rate measured while varying the rotational speed of both the brake disks. It is surprising that both the brake disks draw almost the same amount of cooling flow, following the same linear correlation between the coolant mass flow rate and the rotational speed. This indicates the WBD core (having about 20% less material) can generate a stronger centrifugal force that overcomes the higher pressure drop caused by the WBD core, and thus provide the same suction effect as the pin-finned core.

A multitude of studies have shown that the "staggered" pin fin arrays (from the stationary point of view) arranged in the ventilated channel act as "inline" pin fin arrays in the rotating environment due to the Coriolis effect [12,16–19]. Typically, the staggered array causes a higher pressure drop than the inline array (a 40% higher pressure drop in circular pin fin arrays [33]). Therefore, the centrifugal force of the WBD in the rotating conditions might be stronger than that observed in the stationary conditions. Due to the highly complex, three-dimensional nature of the WBD, the difference in pressure drop between in the stationary and rotating conditions may be insignificant.

4.5.2 Suppression of Dead Flow Regions. The staggered pin–fin arrays (from the stationary point of view) in the ventilated channel act as the "inline" pin fin arrays under the rotating conditions. Large flow separation and a recirculation region exit behind every thick pin fin. These detrimental regions are isolated from each other with little or no interaction. However, in the WBD brake disk, the wake regions behind each thin ligament are narrow. Flow mixing promoted by the three-dimensional morphology of the WBD core may cause strong interaction between these wake regions, which serves to update the fluid in the wake regions, leading partly to the observed enhancement of the overall and local convective heat transfer in the WBD brake disk.

4.5.3 Material Thermophysical Properties. Mild steel (used for the fabrication of the WBD brake disk) has different thermophysical properties from that of cast iron (used for the pin-finned brake disk). Hence, it is necessary to demonstrate that the

observed better cooling performance by the WBD core is not attributable to its distinct thermophysical parameters.

For the transient braking tests, material thermal capacity, and thermal conductivity affect transient thermal behaviors of the brake disks shown in Fig. 8, in addition to convective heat dissipation. The mass of the pin-finned and WBD brake disks was measured to be 14.22 kg and 13.47 kg, respectively. In addition, ductile cast iron has higher specific heat (typically 506 J/(kg K), ASTM A536) than mild steel (typically 481 J/(kg K), SAE1006). Consequently, total thermal capacity of the WBD brake disk is approximately 10% lower than that of the pin-finned brake disk, which tends to hinder the superiority of the WBD brake disk. However, Fig. 8(*b*) shows that the WBD brake disk operates at a lower temperature during the whole braking test, revealing that better cooling performance by the WBD core is not attributable to its distinct thermal capacity.

In terms of material thermal conductivity, transient experimental test of a similar cast iron brake disk by McPhee and Johnson [10] has revealed that material thermal resistance is negligible compared with convective resistance, demonstrating the feasibility of lumped capacitance analysis. For the present braking test concerning average rubbing surface temperature, half the distance between two rubbing surfaces of the cast iron brake disk (i.e., 17 mm) is a reasonable characteristic length to calculate Biot number [10]. At 200 rpm, area-averaged heat transfer coefficient for the pin-finned brake disk was estimated to be 19.4 W/(m^{2}K) according to the effective Nusselt number in Fig. 9. Consequently, Biot number was calculated to be 0.011–0.005 for typical thermal conductivity values of cast iron and mild steel (i.e., 30 W/(mK)−65 W/(mK)). According to Ref. [10], material resistance of the present pin-finned brake disk is also negligible due to a smaller Biot number than 0.1. Hence, if a pin-finned brake disk made of the same mild steel as that used for the WBD brake disk is taken as reference, the superiority of the WBD brake disk approximately remains unchanged.

To further demonstrate the negligible effect of material thermal conductivity on steady-state cooling performance in Fig. 9, steady-state three-dimensional conjugate flow and heat transfer was numerically simulated only for the pin fined brake disk using ANSYS CFX 14.5. The details are not presented here for brevity. After thorough experimental validation, the material thermal conductivity was varied from 30 W/(mK) to 65 W/(mK) in the numerical model to investigate the effect of thermal conductivity, which again covers typical values of cast iron and mild steel. At the maximum rotational speed (i.e., 1000 rpm) within the considered range (i.e., 100 rpm–1000 rpm) when material thermal resistance plays the most pronounced role due to the maximum Biot number, it has been found that the thermal conductivity of the brake disk material (at least within this range) plays negligible part in determining overall heat transfer in the pin-finned brake disk with a deviation of less than 2.5%.

5 Conclusions

This study presented a new class of lightweight ventilated brake disk utilizing a highly porous metallic open cellular core—WBD to further improve the cooling performance of ventilated disk brake systems. A series of transient and steady-state experiments were conducted to characterize its thermofluidic characteristics along with a direct comparison with a commercially available pin-finned brake disk. Conclusions drawn in this study are summarized as follows:

(1) Substantial reduction of rubbing disk temperature (i.e., 16–36%) can be achieved by the WBD core compared to the pin-finned brake disk for the rotational speed ranging from 100 rpm to 1000 rpm.
(2) The three-dimensionally configured thin ligaments of the WBD core lead to azimuthally and radially more uniform heat transfer.
(3) The highly porous WBD core causes higher pressure drop than the pin-finned core but its stronger suction capability gives rise to an equal resultant coolant flow rate for a given rotational speed of the brake disk.
(4) Stronger flow mixing in conjunction with enlarged heat transfer area contributes to the heat transfer enhancement.

Acknowledgment

This research was supported by the International Research & Development Program of the National Research Foundation of Korea (NRF) funded by the Ministry of Education, Science and Technology (MEST) of Korea (Grant No.: K2011-0030886), by the NRF South Africa Incentive Fund for rated researchers, by the National Basic Research Program of China (Grant No.: 2011CB610305) and the Major International Joint Research Program of China (Grant No.: 11120101002).

Nomenclature

A_{in} = flow area of a ventilated channel inlet (m^2)
C = empirical constant in Eq. (11)
d_p = circular pin fin diameter (m)
d_{WBD} = ligament diameter of a WBD core (m)
D_{duct} = inner diameter of a circular intake duct (m)
D_h = hydraulic diameter of a ventilated channel inlet (m)
f_{Dh} = friction factor defined in Eq. (8)
h = overall heat transfer coefficient defined in Eq. (10) (W/m^{2}K)
H_p = pin fin height (m)
H_{h1}, H_{h2} = axial dimensions of a brake hub (m)
H_{WBD} = WBD core height (m)
k = thermal conductivity of air (W/mK)
L = radial distance between two static pressure tappings (m)
l_h = pitch of the helical wire (m)
L_p = pin fin length (m)
L_{WBD} = unit cell length of a WBD core (m)
$\dot{m}$ = cooling flow rate (kg/s)
n = empirical constant in Eq. (11)
N = rotational speed of a brake disk (rpm)
Nu_{Ro} = Nusselt number defined in Eq. (9)
q'' = heat flux released by a heating element (W/m^2)
r = radial coordinate (m)
r_{p1}, r_{p2} = round radii of pin fins (m)
R_{duct} = inner radius of a circular intake duct (m)
R_i = inner radius of a rubbing disk (m)
R_o = outer radius of a rubbing disk (m)
R_{in}, R_{out} = radial locations of pressure tappings (m)
R_{h1}, R_{h2} = radial dimensions of a brake disk hub (m)
R_{p1}–R_{p4} = radial locations of pin fins (m)
Re_{Dh} = Reynolds number defined in Eq. (6)
Re_{Ro} = rotational Reynolds number defined in Eq. (7)
t = time (s)
t_r = rubbing disk thickness (m)
T_{amb} = ambient air temperature (°C)
T_w = disk surface temperature (°C)
$T_{w,m}$ = mean disk surface temperature (°C)
U = axial velocity component in a circular intake duct (m/s)
U_c = centerline velocity of a circular intake duct (m/s)
U_{in} = mean velocity at the inlet of a ventilated channel (m/s)
U_m = mean velocity in a circular intake duct (m/s)
U_o = mid-height radial velocity measured at the exit of a diverging ventilated channel (m/s)
$U_{o,m}$ = mean radial velocity over a traverse line at the outlet of a divergent channel (m/s)
W_p = pin fin width (m)

W_{WBD} = unit cell width of a WBD core (m)
z = axial coordinate (m)

Greek Symbols

Δp = measured pressure drop (Pa)
Δp_r = reversible pressure recovery defined in Eq. (12) (Pa)
ε = porosity of a WBD core
θ = Azimuth coordinate (degree)
μ = dynamic viscosity of air (Pa · s)
ρ = density of air (kg/m^3)
ρ_{SA} = surface area density of a WBD core (m^2/m^3)
ω = angular velocity of a brake disk (rad/s)

Abbreviations

rpm = revolution per minute
WBD = wire-woven bulk diamond

References

[1] Qi, H. S., and Day, A. J., 2007, "Investigation of Disc/Pad Interface Temperatures in Friction Braking," Wear, **262**(5–6), pp. 505–513.
[2] Ahmed, I., Leung, P. S., and Datta, P. K., 2000, "Experimental Investigations of Disk Brake Friction," SAE Paper No. 01-2778.
[3] Cho, M. H., Kim, S. J., Basch, R. H., Fash, J. W., and Jang, H., 2003, "Tribological Study of Gray Cast Iron With Automotive Brake Linings: The Effect of Rotor Microstructure," Tribol. Int., **36**(7), pp. 537–545.
[4] Anoop, S., Natarajan, S., and Kumaresh Babu, S. P., 2009, "Analysis of Factors Influencing Dry Sliding Wear Behaviour of Al/SiC$_p$-Brake Pad Tribosystem," Mater. Des., **30**(9), pp. 3831–3838.
[5] Lee, K., 1999, "Numerical Prediction of Brake Fluid Temperature Rise During Braking and Heat Soaking," SAE Paper No. 1999-01-0483.
[6] Hunter, J. E., Cartier, S. S., Temple, D. J., and Mason, R. C., 1998, "Brake Fluid Vaporization as a Contributing Factor in Motor Vehicle Collisions," SAE Paper No. 980371.
[7] Mackin, T. J., Noe, S. C., Ball, K. J., Bedell, B. C., Bim-Merle, D. P., Bingaman, M. C., Bomleny, D. M., Chemlir, G. J., Clayton, D. B., Evans, H. A., Gau, R., Hart, J. L., Karney, J. S., Kiple, B. P., Kaluga, R. C., Kung, P., Law, A. K., Lim, D., Merema, R. C., Miller, B. M., Miller, T. R., Nielson, T. J., O'Shea, T. M., Olson, M. T., Padilla, H. A., Penner, B. W., Penny, C., Peterson, R. P., Polidoro, V. C., Raghu, A., Resor, B. R., Robinson, B. J., Schambach, D., Snyder, B. D., Tom, E., Tschantz, R. R., Walker, B. M., Wasielewski, K. E., Webb, T. R., Wise, S. A., Yang, R. S., and Zimmerman, R. S., 2002, "Thermal Cracking in Disc Brakes," Eng. Failure Anal., **9**(1), pp. 63–76.
[8] Kao, T. K., Richmond, J. W., and Douarre, A., 2000, "Brake Disc Hot Spotting and Thermal Judder: An Experimental and Finite Element Study," Int. J. Veh. Des., **23**(3–4), pp. 276–296.
[9] Johnson, D. A., Sperandei, B. A., and Gilbert, R., 2003, "Analysis of the Flow Through a Vented Automobile Brake Rotor," ASME J. Fluids Eng., **125**(6), pp. 979–986.
[10] McPhee, A. D., and Johnson, D. A., 2008, "Experimental Heat Transfer and Flow Analysis of a Vented Brake Rotor," Int. J. Therm. Sci., **47**(4), pp. 458–467.
[11] Galindo-Lopez, C. H., and Tirovic, M., 2008, "Understanding and Improving the Convective Cooling of Brake Discs With Radial Vanes," IMechE J. Automob. Eng., **222**(7), pp. 1211–1229.
[12] Reddy, S. M., Mallikarjuna, J. M., and Ganesan, V., 2008, "Flow and Heat Transfer Analysis of a Ventilated Disc Brake Rotor Using CFD," SAE Paper No. 2008-01-0822.
[13] Nejat, A., Aslani, M., Mirzakhalili, E., and Najian Asl, R., 2011, "Heat Transfer Enhancement in Ventilated Brake Disk Using Double Airfoil Vanes," ASME J. Therm. Sci. Eng. Appl., **3**(4), p. 045001.
[14] Daudi, A. R., 1999, "72 Curved Fins and Air Director Idea Increases Airflow Through Brake Rotors," SAE Paper No. 1999-01-0140.
[15] Daudi, A. R., 1999, "72 Curved Fin Rotor Design Reduces Maximum Rotor Temperature," SAE Paper No. 1999-01-3395.
[16] Wallis, L., Leonardi, E., Milton, B., and Joseph, P., 2002, "Air Flow and Heat Transfer in Ventilated Disc Brake Rotors With Diamond and Tear-Drop Pillars," Numer. Heat Transfer, Part A, **41**(6–7), pp. 643–655.
[17] Wallis, L., 2003, "A Comparison of Bi-Directional Disc Brake Rotor Passage Designs," Ph.D. thesis, University of New South Wales, Sydney, Australia.
[18] Palmer, E., Mishra, R., and Fieldhouse, J., 2008, "A Computational Fluid Dynamic Analysis on the Effect of Front Row Pin Geometry on the Aerothermodynamic Properties of a Pin-Vented Brake Disc," IMechE J. Automob. Eng., **222**(7), pp. 1231–1245.
[19] Palmer, E., Mishra, R., and Fieldhouse, J., 2009, "An Optimization Study of a Multiple-Row Pin-Vented Brake Disc to Promote Brake Cooling Using Computational Fluid Dynamics," IMechE J. Automob. Eng., **223**(7), pp. 865–875.
[20] Wadley, H. N. G., 2006, "Multifunctional Periodic Cellular Metals," Philos. Trans. R. Soc., A, **364**(1838), pp. 31–68.
[21] Lee, Y.-H., Lee, B.-K., Jeon, I., and Kang, K.-J., 2007, "Wire-Woven Bulk Kagome Truss Cores," Acta Mater., **55**(18), pp. 6084–6094.
[22] Lee, M.-G., Ko, G.-D., Song, J., and Kang, K.-J., 2012, "Compressive Characteristics of a Wire-Woven Cellular Metal," Mater. Sci. Eng. A, **539**, pp. 185–193.
[23] Kim, T., Zhao, C. Y., Lu, T. J., and Hodson, H. P., 2004, "Convective Heat Dissipation With Lattice-Frame Materials," Mech. Mater., **36**(8), pp. 767–780.
[24] Joo, J.-H., Kang, K.-J., Kim, T., and Lu, T. J., 2011, "Forced Convective Heat Transfer in All Metallic Wire-Woven Bulk Kagome Sandwich Panels," Int. J. Heat Mass Transfer, **54**(25), pp. 5658–5662.
[25] Feng, S. S., Li, M. Z., Joo, J.-H., Kang, K.-J., Kim, T., and Lu, T. J., 2012, "Thermomechanical Properties of Brazed Wire-Woven Bulk Kagome Cellular Metals for Multifunctional Applications," J. Thermophys. Heat Transfer, **26**(1), pp. 66–74.
[26] Limpert, R., 1975, "Cooling Analysis of Disc Brake Rotors," SAE Paper No. 751014.
[27] Sisson, A. E., 1978, "Thermal Analysis of Vented Brake Rotors," SAE Paper No. 780352.
[28] Sweet, J. N., Roth, E. P., and Moss, M., 1987, "Thermal Conductivity of Inconel 718 and 304 Stainless Steel," Int. J. Thermophys., **8**(5), pp. 593–606.
[29] Lyall, M. E., 2006, "Heat Transfer From Low Aspect Ratio Pin Fins," Master thesis, Virginia Polytechnic Institute and State University, Blacksburg, VA.
[30] Barigozzi, G., Cossali, G. E., Perdichizzi, A., Boden, A., and Pacchiana, P., 2002, "Experimental Investigation of the Mean and Turbulent Flow Characteristics at the Exit of Automotive Vented Brake Discs," SAE Paper No. 2002-01-2590.
[31] Coleman, H. W., and Steele, W. G., 2009, *Experimentation, Validation, and Uncertainty Analysis for Engineers*, 3rd ed., Wiley, Hoboken, NJ.
[32] Jerhamre, A., and Bergström, C., 2001, "Numerical Study of Brake Disc Cooling Accounting for Both Aerodynamic Drag Force and Cooling Efficiency," SAE Paper No. 2001-01-0948.
[33] Kim, T., and Lu, T. J., 2008, "Pressure Drop Through Anisotropic Porous Mediumlike Cylinder Bundles in Turbulent Flow Regime," ASME J. Fluids Eng., **130**(10), p. 104501.
[34] Tian, J., Kim, T., Lu, T. J., Hodson, H. P., Queheillalt, D. T., Sypeck, D. J., and Wadley, H. N. G., 2004, "The Effects of Topology Upon Fluid-Flow and Heat-Transfer Within Cellular Copper Structures," Int. J. Heat Mass Transfer, **47**(14), pp. 3171–3186.